

Time-Bin and Polarization Superdense Teleportation for Space Applications

Joseph C. Chapman^{1,2,*}, Trent M. Graham^{2,3}, Christopher K. Zeidler^{1,2}, Herbert J. Bernstein⁴, and Paul G. Kwiat^{1,2}

¹*Illinois Quantum Information Science and Technology Center, University of Illinois at Urbana-Champaign, Urbana, Illinois 61801, USA*

²*Department of Physics, University of Illinois at Urbana-Champaign, Urbana, Illinois 61801, USA*

³*Department of Physics, University of Wisconsin - Madison, Madison, Wisconsin 53706, USA*

⁴*Institute for Science & Interdisciplinary Studies & School of Natural Sciences, Hampshire College, Amherst, Massachusetts 01002, USA*



(Received 5 September 2019; revised 8 January 2020; accepted 18 May 2020; published 15 July 2020)

To build a global quantum-communication network, low-transmission, fiber-based communication channels can be supplemented by using a free-space channel between a satellite and a ground station on Earth. We construct a system that generates hyperentangled photonic “ququarts” and measures them to execute multiple quantum-communication protocols of interest. We successfully execute and characterize superdense teleportation, a modified remote-state preparation protocol that transfers more quantum information than standard teleportation, for the same classical information cost, and moreover, is in principle deterministic. Our measurements show an average fidelity of 0.94 ± 0.02 , with a phase resolution of approximately 7° , allowing reliable transmission of $> 10^5$ distinguishable quantum states. Additionally, we demonstrate the ability to compensate for the Doppler shift, which would otherwise prevent sending time-bin encoded states from a rapidly moving satellite, thus allowing the low-error execution of phase-sensitive protocols during an orbital pass. Finally, we show that the estimated number of received coincidence counts in a realistic implementation is sufficient to enable faithful reconstruction of the received state in a single pass.

DOI: [10.1103/PhysRevApplied.14.014044](https://doi.org/10.1103/PhysRevApplied.14.014044)

I. INTRODUCTION

A global quantum network would have myriad uses. For example, it could improve the collective computational power of quantum computers by allowing them to communicate [1], enable arbitrarily long-distance secure communication using quantum cryptography [2], and might even facilitate planet-scale distributed quantum sensors, e.g., for clock synchronization [3], and superresolution telescopes [4–6]. Currently, the distance between nodes in a potential quantum network is limited by the absorption loss in fiber-optic cables or the effects of turbulence for free-space terrestrial channels. If a channel between a satellite and Earth are used as part of the network, the distances between nodes could be greatly increased because that channel is less affected by the above limiting factors [7]. The utility of a free-space satellite-Earth channel has been recognized by many research groups around the world [8]. For example, the Chinese Micius satellite was used to demonstrate long-distance photonic-entanglement distribution [9], one version of quantum key distribution (QKD) [10,11], and a

preliminary test of quantum teleportation [12]. Additionally, there is significant work ongoing in Singapore [13], Italy [14], Canada [15], and Austria [11,16].

To further the development of quantum-communication applications in space, we create a system that can execute multiple quantum-communication protocols, including high-dimensional entanglement-based quantum key distribution [17], superdense teleportation (SDT) [18], and high-dimensional Bell inequality and quantum steering tests [19]. With additional modifications, the system could be suitable for operation on a satellite. In this work, we characterize our source of hyperentangled photons and the performance of SDT in our system over its whole message space, and demonstrate through lab test and calculation the ability to robustly execute SDT during a single orbital pass of a low-earth orbit satellite, e.g., the International Space Station (ISS). This work significantly exceeds previous SDT work [20] by the authors, due to incorporation of robust quantum degrees of freedom and elimination of encoding in nonrobust degrees of freedom, compensation for the Doppler shift (which otherwise renders the protocol useless), and a more thorough characterization of the SDT system in general; we also incorporate a comparison

*jchapmn2@illinois.edu

between the standard maximum-likelihood analysis and Bayesian analysis methods that are superior to standard quantum-state tomography techniques for low-rate communications. Finally, we undertake a thorough analysis to project rates and performance in a low-earth-orbit demonstration of this protocol.

II. SUPERDENSE TELEPORTATION PROTOCOL

SDT, as shown in Fig. 1, is a three-party protocol involving Alice, Bob, and Charles. Charles wants to send Bob an “equimodular” quantum state—a subset of the states in the available Hilbert space, in which all terms have the same magnitude:

$$|\Psi_C\rangle = \frac{1}{\sqrt{d}}(|0\rangle + e^{i\phi_1}|1\rangle + e^{i\phi_2}|2\rangle + \dots + e^{i\phi_{d-1}}|(d-1)\rangle) \quad (1)$$

for any values of $\phi_1, \phi_2, \dots, \phi_{d-1} \in [0, 2\pi)$. To begin the protocol, Bob and Charles share a d -dimensional maximally entangled state:

$$|\Psi_{BC}\rangle = \frac{1}{\sqrt{d}}[|00\rangle + |11\rangle + |22\rangle + \dots + |(d-1)(d-1)\rangle], \quad (2)$$

onto which Charles locally encodes his desired phases:

$$|\Psi_{BC}\rangle = \frac{1}{\sqrt{d}}[|00\rangle + e^{i\phi_1}|11\rangle + e^{i\phi_2}|22\rangle + \dots + e^{i\phi_{d-1}}|(d-1)(d-1)\rangle]. \quad (3)$$

Next, Alice measures Charles’ photon in a mutually unbiased basis from the one in which Charles applied the

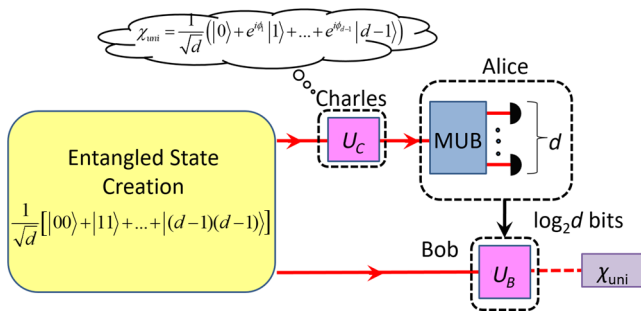


FIG. 1. Superdense teleportation: Charles desires to send Bob a d -dimensional equimodular state. To do so via SDT, Charles and Bob start by sharing a d -dimensional maximally entangled state; Charles makes local unitary operations to set the desired phases of the equimodular state. Alice then makes a measurement in a mutually unbiased basis to the basis Charles applied his phases in. Her measurement outcome is transmitted to Bob, who then makes the necessary unitary transformation to deterministically convert his half of the entangled pair into the precise state Charles wanted to send.

phases, e.g., the basis

$$|A_1\rangle \equiv \frac{1}{2}(+|0\rangle + |1\rangle + |2\rangle - |3\rangle), \quad (4)$$

$$|A_2\rangle \equiv \frac{1}{2}(+|0\rangle + |1\rangle - |2\rangle + |3\rangle), \quad (5)$$

$$|A_3\rangle \equiv \frac{1}{2}(+|0\rangle - |1\rangle + |2\rangle + |3\rangle), \quad (6)$$

$$|A_4\rangle \equiv \frac{1}{2}(-|0\rangle + |1\rangle + |2\rangle + |3\rangle), \quad (7)$$

where we now restrict our discussion to $d = 4$, relevant for our experimental implementation. States $|A_1\rangle$ to $|A_4\rangle$ are those projected onto by Alice’s four detectors. Before Alice’s measurement, the full state of the system is given by

$$\begin{aligned} |\Psi_{AB}\rangle = & \frac{1}{2} \left[\frac{1}{2} |A_1\rangle \otimes (+|0\rangle + e^{i\phi_1}|1\rangle + e^{i\phi_2}|2\rangle - e^{i\phi_3}|3\rangle) \right. \\ & + \frac{1}{2} |A_2\rangle \otimes (+|0\rangle + e^{i\phi_1}|1\rangle - e^{i\phi_2}|2\rangle + e^{i\phi_3}|3\rangle) \\ & + \frac{1}{2} |A_3\rangle \otimes (+|0\rangle - e^{i\phi_1}|1\rangle + e^{i\phi_2}|2\rangle + e^{i\phi_3}|3\rangle) \\ & \left. + \frac{1}{2} |A_4\rangle \otimes (-|0\rangle + e^{i\phi_1}|1\rangle + e^{i\phi_2}|2\rangle + e^{i\phi_3}|3\rangle) \right]. \end{aligned} \quad (8)$$

Upon measurement, Alice sends her result to Bob (using two classical bits of information), who then applies the correct unitary transformation (a π -phase shift on one of the four terms) so that [21]

$$|\Psi_B\rangle = |\Psi_C\rangle = \frac{1}{2}(|0\rangle + e^{i\phi_1}|1\rangle + e^{i\phi_2}|2\rangle + e^{i\phi_3}|3\rangle). \quad (9)$$

Although the SDT state space is restricted to equimodular states, and is therefore not suitable for general quantum computation, these states are sufficient to enable blind quantum computing, a client-server cluster quantum-computing model that ensures privacy of the inputs, the outputs, and the computation being performed [22]. Moreover, the SDT protocol is deterministically successful, in contrast to quantum teleportation and probabilistic remote-state preparation, which both only succeed at most half of the time using linear optics [20]. In addition, it also uses fewer classical communication resources than quantum teleportation and deterministic remote-state preparation [20]; for example, whereas standard teleportation requires Alice to send two classical bits to teleport

a single qubit (described by two continuous variables, e.g., $|\psi\rangle = \cos\theta|0\rangle + \sin\theta e^{i\phi}|1\rangle$), SDT transmits three continuous variables for the same two classical bits. Higher-dimensional quantum teleportation has been performed before but with lower fidelity and only probabilistic success [23,24]. Furthermore, Alice's measurements for SDT are substantially less resource intensive than those needed, e.g., for remote-state preparation [20]; this is an important consideration for a satellite-based protocol.

III. SDT PROTOCOL EXECUTION

Superdense teleportation has been executed previously using photons hyperentangled in their polarization and orbital angular momentum (OAM) [20]. For our intended goal of transmitting quantum information over a channel from space to earth, time bins are a much better choice than OAM modes, as the latter are corrupted by atmospheric turbulence and require larger apertures to faithfully detect [25]. Using nondegenerate spontaneous parametric down-conversion, our source produces time-bin and polarization-entangled photons (see Appendix A) in the 16-dimensional equimodular state

$$|\Psi_{BC}\rangle = \frac{1}{2} [|(Ht_1)_{810}(Ht_1)_{1550}\rangle + |(Vt_1)_{810}(Vt_1)_{1550}\rangle + |(Ht_2)_{810}(Ht_2)_{1550}\rangle + |(Vt_2)_{810}(Vt_2)_{1550}\rangle]. \quad (10)$$

Here H and V refer to horizontal and vertical polarization, t_1 and t_2 refer to two time bins, and 810 and 1550 (nm) are the photon wavelengths. As shown in Fig. 2, the 810-nm (1550-nm) photon is distributed to Charles (Bob), who applies phases ϕ_{LC_A} , ϕ_{LC_B} , and ϕ_{LC_C} on the state by actuating three different liquid crystals, LC_A , LC_B , and LC_C ,

to allow arbitrary phase selection over the range $[0, 2\pi)$. Alice's projective measurement in a mutually unbiased basis is carried out by the polarizing beam splitter (PBS) of her interferometer, preceded by half-wave plate (HWP₁) and HWP₂ in the interferometer arms, which effectively place the PBS into the diagonal or antidiagonal basis. Similarly, HWP₃ and HWP₄ are oriented at 22.5° with respect to horizontal, so the detectors project onto a superposition of time bins. Instead of having Bob complete the protocol by making the necessary unitary transformation, Bob measures four tomographies, conditioned on which of Alice's detectors fires. This allows us to tomographically reconstruct all four of the different states sent to Bob and apply the unitary transformation during the analysis after state reconstruction.

IV. RESULTS

To verify the quality of our source, we perform a full tomography of the joint state of the system by performing 1296 measurements (six measurements for each qubit in the ququart). This involved adding extra half- and quarter-wave plates (QWP) and a removable polarizer into Alice and Charles' side so a complete tomography could be made on each photon of the pair; see Appendix 4 for details. The purity of the reconstructed density matrix (Fig. 3) is $P \equiv \text{Tr}\rho^2 = 0.932 \pm 0.007$; the fidelity of the absolute value of the reconstructed density matrix, $|\rho_m|$, with Eq. (10) is

$$F = \left(\text{Tr} \sqrt{\rho_{BC}^{1/2} |\rho_m| \rho_{BC}^{1/2}} \right)^2 = 0.955 \pm 0.004. \quad (11)$$

For each calculation, the error bar is produced from a Monte Carlo analysis, assuming Poissonian counting

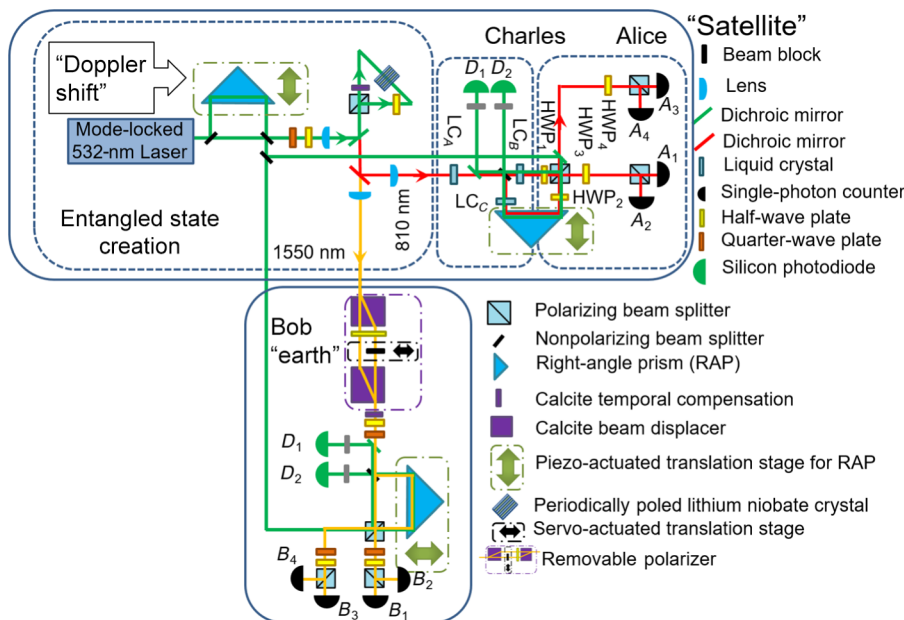


FIG. 2. Superdense teleportation optical setup: Photonic time-bin and polarization ququarts are generated via spontaneous parametric down-conversion in periodically poled lithium niobate (See Appendix A). Green lines are the 532-nm pump (and stabilization) beam; red and yellow are the signal (810 nm) and idler (1550 nm) photons, respectively. Each half of the ququart is manipulated and measured independently via Alice/Charles' and Bob's sections, which include full polarization analysis, complete phase manipulation, and an unbalanced interferometer to allow measurements of superpositions of time bins.

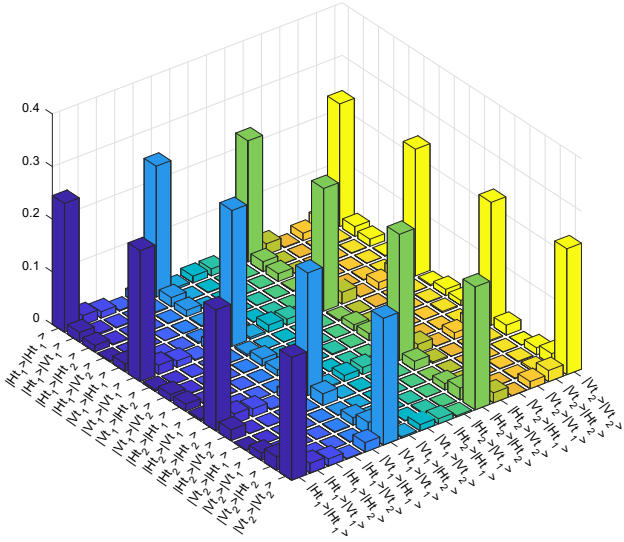


FIG. 3. Hyperentangled state density matrix: absolute value of the reconstructed hyperentangled state density matrix, with a fidelity of 0.955 ± 0.004 with the desired state, and a purity of 0.932 ± 0.007 .

statistics and using 100 samples, with mean count values on the order of the number of detected events for each of the tomography measurements (see Appendix D, Table III).

A. Phase space characterization

To characterize the performance of the SDT protocol over the complete space of possible states (any value of ϕ_1 , ϕ_2 , and $\phi_3 \in [0, 2\pi)$), we measure every combination of ϕ_1 , ϕ_2 , and ϕ_3 at roughly 45° intervals between $[0, 2\pi)$. These 512 states are represented in phase space in Fig. 4 for trials where Alice obtained a click at detector A_1 (which is representative of events detected by the other three detectors). More precisely, the plots show the difference between the phases of the reconstructed state ($\phi_{1,\text{meas}}$, $\phi_{2,\text{meas}}$, and $\phi_{3,\text{meas}}$) and the calibration phases ($\phi_{1,\text{calib}}$, $\phi_{2,\text{calib}}$, and $\phi_{3,\text{calib}}$) from a calibration tomography taken every four tomographies. The phases between the polarizations are relatively stable and do not need to be measured except when the alignment changes, but the time-bin phase is more susceptible to slight phase drift. We believe the increased variation in $\phi_{LC_A} + \phi_{LC_B}$ (top-left graph of Fig. 4) is due to the compounded variation in ϕ_{LC_A} and ϕ_{LC_B} as ϕ_{LC_A} , the phase that changes within each grouping in the projections of Fig. 4, is increased. The average fidelity over the entire grid and all of Alice's detectors is

$$F = \left(\text{Tr} \sqrt{\rho_{\text{tar}}^{1/2} \rho_{\text{meas}} \rho_{\text{tar}}^{1/2}} \right)^2 = 0.94 \pm 0.02, \quad (12)$$

where $\rho_{\text{tar}} = |\Psi_{\text{tar}}\rangle\langle\Psi_{\text{tar}}|$ and

$$|\Psi_{\text{tar}}\rangle = \frac{1}{2} [|0\rangle + e^{i(\phi_{1,\text{tar}})} |1\rangle + e^{i(\phi_{2,\text{tar}})} |2\rangle + e^{i(\phi_{3,\text{tar}})} |3\rangle]. \quad (13)$$

Here

$$\phi_{1,\text{tar}} \equiv \phi_{1,\text{calib}} + \phi_{LC_A} + \phi_{LC_B}, \quad (14)$$

$$\phi_{2,\text{tar}} \equiv \phi_{2,\text{calib}} - \phi_{LC_C}, \quad (15)$$

$$\phi_{3,\text{tar}} \equiv \phi_{3,\text{calib}} + \phi_{LC_A}. \quad (16)$$

From the grids in Fig. 4, we calculate the standard deviation of $\Delta\phi_i \equiv \phi_{i,\text{meas}} - \phi_{i,\text{tar}}$, averaging over all three phases, to be 9° , while the mean is only 3° . We estimate 3° of the standard deviation is from Poisson statistical fluctuations and alignment drift in the setup over time.

To further assess errors, we repeat the measurement eight times for every combination of ϕ_1 , ϕ_2 , and ϕ_3 at roughly 90° intervals between $[0, 2\pi)$; allowing us to plot a grid of the average phase measured at each point (see Appendix D, Fig. 10). From these data, we calculate the mean and standard deviation of $\Delta\phi$ to be 4° and 10° , respectively. Additionally, the average fidelity of the measured state with each target over the entire grid, including all four of Alice's measurement outcomes, is $F = 0.93 \pm 0.03$. We identify some of the causes of infidelity in our system to be imperfect phase setting, imperfect phase stabilization, different measurement efficiency for the different tomography measurements, and nonequal magnitudes of the terms in the superposition; see Appendix 3 for quantitative estimates of these effects.

In order to further assess the resolving power of our system to distinguish states with nearby phase values, for each phase (ϕ_1 , ϕ_2 , and ϕ_3), we create two distributions (two liquid-crystal settings) of ten samples each, corresponding to phases differing by 7° on average; we then apply a two-sample Kolmogorov-Smirnov (KS) test [26] to test the null hypothesis (once for each phase) that all 20 samples are from the same distribution (liquid-crystal setting), concluding that we can reject the null hypothesis that the data are drawn from a single distribution with $\alpha = 0.05$, in other words, with a 5% probability of wrongly rejecting the null hypothesis; see Appendix F for more information. Thus, we can estimate the total number of resolvable teleported quantum states with our system to be $(360^\circ/7^\circ)^3 \approx 136\,000$.

B. Doppler shift compensation

Because a low-earth orbit (LEO) satellite travels at $V_r \sim 8$ km/s, the source will have moved non-negligibly

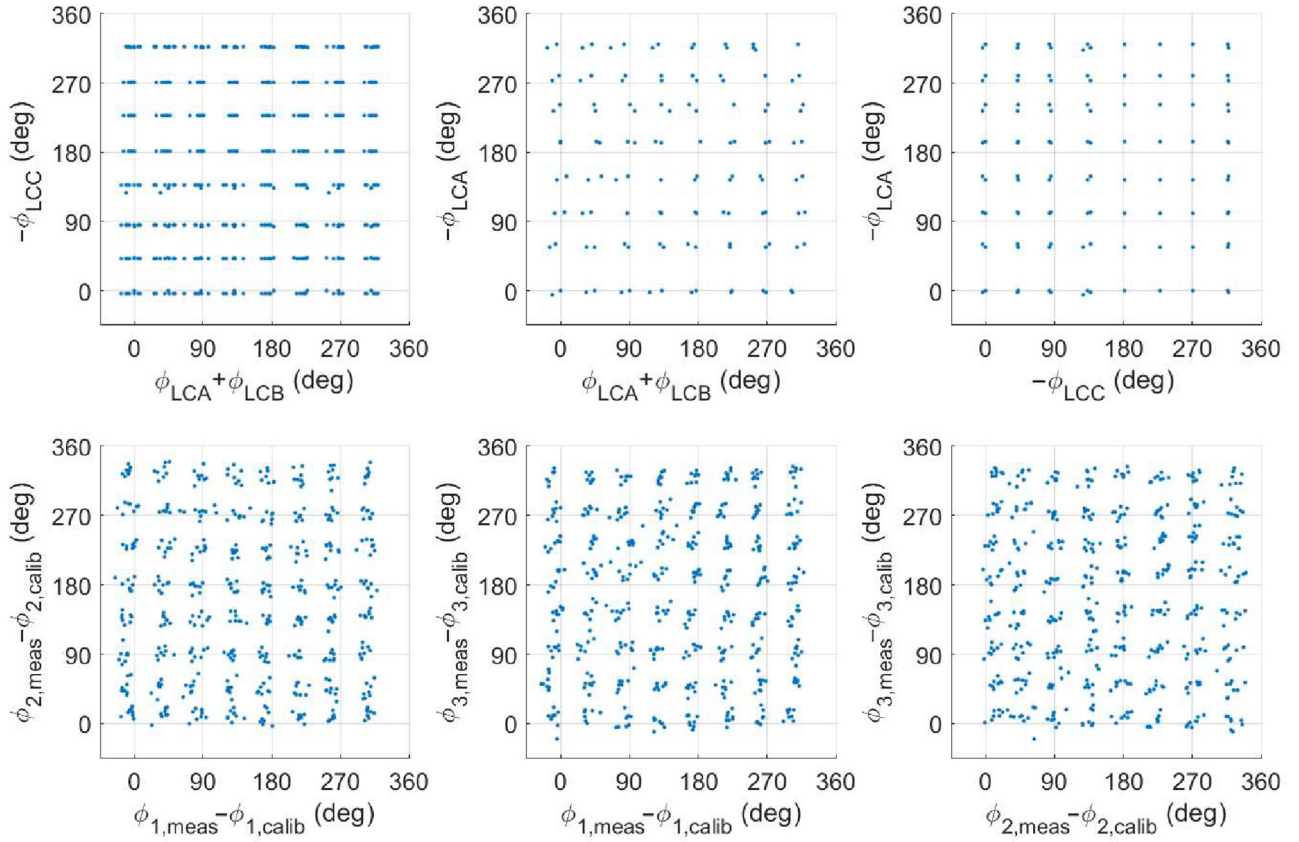


FIG. 4. Projections onto 45° grid. (Top row) Target projections based on liquid-crystal phase calibration. (Bottom row) Measured phase projections after subtracting calibrated phase offset.

between the times when the early and late time bins are transmitted. As the satellite approaches (recedes) this shortens (lengthens) the interval between emitted time bins from the Earth's reference frame. Uncorrected, the corresponding variation in phase [between the first two and last two terms in the state from Eq. (10)] would completely obscure the phases Charles is attempting to teleport to Bob: a variation of about 80 radians is expected, depending on the time-bin separation and the orbit elevation angle. See Appendix G for more information. To keep this

Doppler shift (and any other time-varying phase shifts) from adversely affecting the protocol's performance, we develop a phase compensation system that uses a classical laser beam and proportional-integral feedback [27] to stabilize the path-length difference of the interferometers. Figure 5 shows the performance of the classical stabilization system while a continuously varying, lab-simulated Doppler shift, matching that expected in a typical satellite orbit, is imposed. The standard deviation of the phase with the stabilization active is 1.3° .

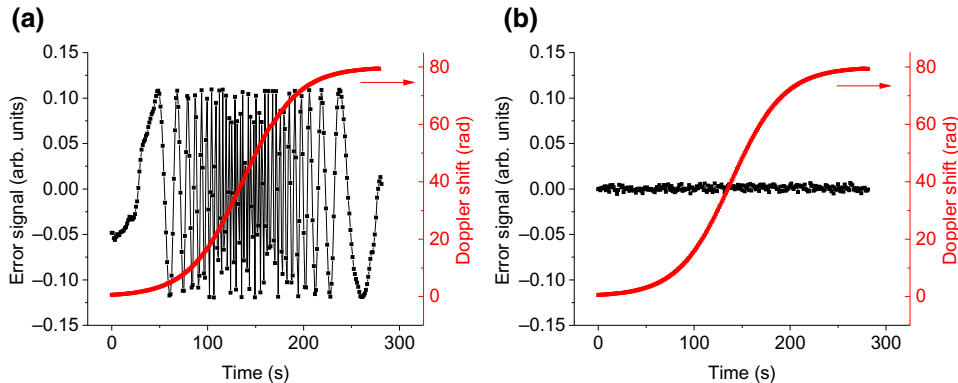


FIG. 5. Classical Doppler shift stabilization: (a) With phase stabilization off, the error signal sweeps through many interferometric fringes. (b) With phase stabilization on, the error signal is nearly constant, corresponding to $\Delta\phi = \pm 1.3^\circ$.

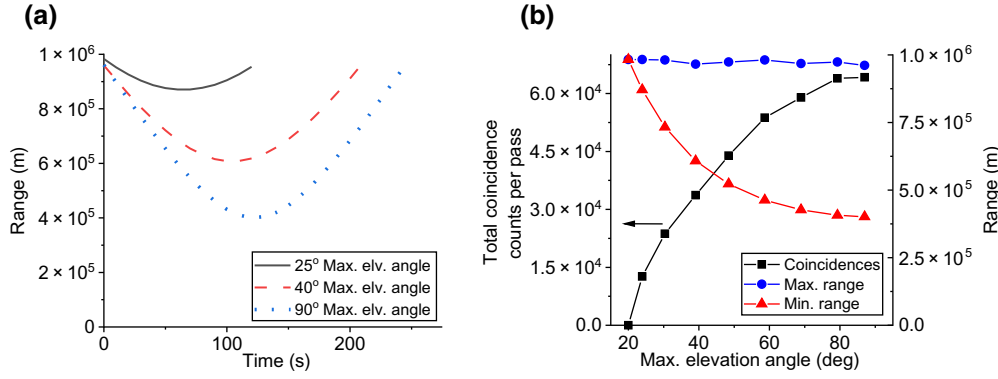


FIG. 6. Link analysis calculations. (a) Range of the satellite to a ground station at 39° N latitude with an approximately 25° (solid black line), approximately 40° (dashed red line), and approximately 90° (dotted blue line) maximum elevation angle during the pass. (b) On the left vertical axis, we plot the estimated total number of collected coincidence counts per orbital pass versus the maximum elevation angle of that pass (see text for underlying assumptions); on the right vertical axis, we plot the minimum and maximum range of the satellite per orbital pass.

We measure nine tomographies while executing SDT for the same choice of ϕ_1 , ϕ_2 , and ϕ_3 . Without phase stabilization, we obtain an average fidelity $F = 0.53 \pm 0.06$; with the phase stabilization turned on, we obtain an average fidelity $F = 0.92 \pm 0.02$ and $\Delta\phi$ have a standard deviation of 14° . We suspect the cause of the increased phase variation during the Doppler shift to be relative drift between the path lengths of Alice and Charles' and Bob's interferometers while the Doppler shift is taking place. This should not occur during an actual implementation in space, because a Doppler shift would not occur on the time bins sent from the pump to Alice and Charles' interferometer (which is on the same platform as the source); only those sent to Bob's interferometer would experience a Doppler shift.

C. Link analysis

The maximum elevation angle of a LEO satellite with respect to a ground station on Earth varies from pass to pass, and the instantaneous elevation angle (defined as the angle between the horizon and the satellite) changes as the satellite passes overhead, leading to a change in the separation between the satellite and ground terminal—the “range” [Fig. 6(a)]. With that in mind, displayed in Fig. 6(b), we calculate the estimated total coincidence counts per pass, maximum range per pass, and minimum range per pass versus maximum elevation angle per pass, assuming the minimum acceptable elevation angle during a pass is 20° [which fixes the maximum range to around 10^6 m, as seen in Fig. 6(b)]. For these calculations, we use simulated orbit data for all orbital parameters—the simulated satellite orbit had a 400-km altitude and 51° inclination (appropriate, e.g., for the ISS), and the range as a function of time is calculated from the satellite to a ground station located at 39° N latitude; see Fig. 6(a) for example data. The Friis equation $\{\eta(r) = [\pi D_T D_R / (4\lambda r)]^2\}$ to

estimate channel transmission η as a function of range r [28,29] is numerically integrated over the whole pass (for transmitting telescope diameter $D_T = 0.1$ m, receiving telescope diameter $D_R = 1$ m, and wavelength $\lambda = 1550$ nm, with the added assumptions of a 6-dB loss for combined receiver telescope [30] and adaptive optics system single-mode fiber collection efficiency [31], and 4-dB loss for an estimate of the analysis and detection system transmission), and assuming a 400-MHz repetition rate pump laser, pair production probability of 0.01 per pump pulse, and a 4-dB loss from the analysis and detection system in space. This experiment would require an adaptive optics correction system so the collected light can be efficiently coupled into a single-mode fiber before entering Bob's analysis and detection system. With this requirement, any turbulence is effectively converted to a reduction in transmission.

All tomographies analyzed thus far in the paper used maximum-likelihood estimation (MLE) [32]. We also analyze some tomographic data using a Bayesian-mean-estimation (BME) approach [33], computing the representative state as an average over all states, weighted by the likelihood that a state produced the data observed. Using MLE yields results that are biased towards pure states [34], and this effect becomes more significant when the data used for the tomography has fewer counts, as can be seen in the low-count regime in Fig. 7. In these low-count regimes, using BME leads to results that are more reflective of the data measured. However, analyzing tomographic data using BME is more computationally intensive, especially when more than several hundred coincidence counts are collected, so MLE is often preferred with higher counts because the resultant difference between BME and MLE becomes small.

SDT is not inherently affected by source brightness except for slight degradation in purity from multiple

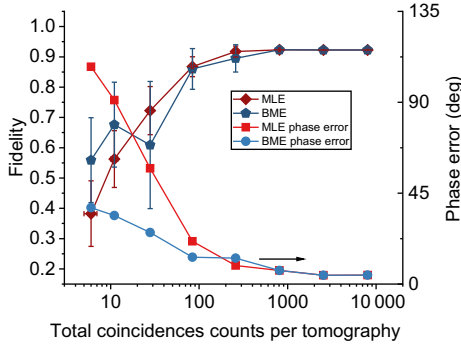


FIG. 7. Required counts for high-fidelity SDT. The fidelity of the reconstructed state using MLE and BME, and the phase error (the standard deviation of $\Delta\phi_i \equiv \phi_{i,\text{meas}} - \phi_{i,\text{tar}}$, averaging over all three phases), as a function of the total number of coincidence counts collected per a 36-setting tomography. The fidelity and phase error is averaged over all four of the states produced by the different projections of Alice's detectors, A_1 – A_4 .

pair events [35]; however, to verify that the protocol is operating successfully, one needs to take a tomography of the received photons contingent on which state Alice measured (A_1 – A_4); such conditional tomography is required because we are not yet implementing the final active feed-forward step of the full SDT protocol. We know from previous analysis [35] that only approximately 300 coincidence counts total per the 36 tomography measurements are needed for a reliable reconstruction (state fidelity > 0.9) using MLE. From our calculations above, all passes above 25° maximum elevation angle should produce more than 10 000 total coincidence counts per pass (Fig. 6). Therefore, under those assumptions, a future implementation of this system in space should produce and measure more than enough coincidences to verify an implementation of SDT in a single pass. Furthermore, with currently available technology, such as adaptive optics on receiver telescopes for single-mode fiber coupling, active polarization compensation to ensure Bob and Charles have a common basis, and time-bin phase stabilization as demonstrated in this work, SDT should be implementable in a space-to-earth channel without degradation compared to our laboratory implementation.

V. CONCLUSIONS

We show a systematic characterization of our system to execute SDT, and characterize the full volume of accessible quantum states by measuring the fidelity of states at regular intervals of phase. The phase error is measured from this characterization, along with the distinguishability of closely spaced phases. We also demonstrate the ability to operate during a Doppler shift by employing an active feedback system. Lastly, we calculate the expected coincidence counts for a range of satellite orbital passes and

show that for nearly all of them we should have ample counts to reconstruct the received state faithfully.

The value in quantum communication occurs when two remote parties can coordinate to achieve some desirable task beyond the capabilities of classical communication. Because SDT transmits only a restricted space of states, one might worry that the protocol would be insufficiently versatile to enable interesting or useful quantum-processing tasks. However, the equimodular states of SDT enable high-dimensional entanglement-based quantum cryptography [17]; moreover, they are just the type required for quantum fingerprinting [36] and for blind quantum computing [22]. Therefore, a space-to-earth implementation of SDT would be an enabling demonstration along the path toward a useful global quantum network.

ACKNOWLEDGMENTS

The authors acknowledge Alexander Hill for the suggestion to use a two-sample KS test. Thanks to MIT-Lincoln Laboratory for the orbital simulation calculations. This work is primarily supported by NASA Grant No. NNX13AP35A and NASA Grant No. NNX16AM26G. This work is also supported by a DoD, Office of Naval Research, National Defense Science and Engineering Graduate Fellowship (NDSEG). All authors contributed to experiment design and commented on the paper. H.B. conceptualized SDT protocol. T.G. constructed the initial optical system and wrote the preliminary version of the tomography analysis code. C.K.Z. started upgrade of detection system, implemented Bayesian analysis, and calculated the tomography settings and the contributions to the loss of fidelity. J.C.C. upgraded the optical system and finished upgrade of detection system, and carried out all experiments and MLE data analysis. J.C.C., C.K.Z., and P.G.K. wrote the manuscript.

APPENDIX A: STATE GENERATION AND DETECTION

To create the photons entangled in polarization and time bin, an 80-MHz mode-locked 532-nm laser (frequency doubled from 1064 nm, Spectra Physics Vanguard 2.5W 355 laser) with a pulse width approximately 7 ps is sent through an approximately 2.4-ns delay to split every pump pulse into an early and late pulse, each of which coherently pumps the polarization entanglement source [37], a polarizing Sagnac interferometer with a Fresnel rhomb [used as a broadband half-wave plate], type-0 periodically poled (poling period is $7.5 \mu\text{m}$) lithium niobate crystal, and a calcite crystal (to compensate for dispersion); the horizontal (vertical) component of the diagonally polarized pump travels (counter)clockwise through the Sagnac. Neglecting time bins, traversing the two paths of the interferometer

corresponds to this transformation [38,39]:

$$\frac{(|H\rangle_{532} + |V\rangle_{532})}{\sqrt{2}} \Rightarrow \frac{(|V\rangle_{810}|V\rangle_{1550} + |H\rangle_{810}|H\rangle_{1550})}{\sqrt{2}}, \quad (\text{A1})$$

where the subscripts are nominal central wavelengths of the photons. Sending a superposition of time bins into the polarizing Sagnac results in the state Eq. (10) of the main text.

The 532-nm pump bandwidth is 64 GHz. The down-conversion bandwidth is measured by stimulated down-conversion (difference-frequency generation) between a tunable 1550-nm laser and the pump [40]. The tunable 1550-nm laser is swept and a peak in the collected 810-nm counts is recorded. The peak is centered at 1551 nm (corresponding to 809.7 nm for the conjugate photons), with a full-width at half-maximum width of 1.5 nm (0.4 nm) [21].

Due to birefringence, $|H\rangle$ and $|V\rangle$ do not exit the Sagnac source at exactly the same time. To compensate for this we insert 0.5-mm of a-cut calcite into the 1550-nm beam path. This increased the visibility in the diagonal polarization basis from 91 to 98%.

For Charles to encode his desired phases, he uses LC_A , LC_B , and LC_C , with their fast axes located along the horizontal, horizontal, and vertical axes, respectively, to allow arbitrary phase selection over the range $[0, 2\pi)$.

The 810-nm photons are detected by four avalanche photodiodes (Excelitas SPCM-AQ4C) with efficiency approximately 45%. The 1550-nm photons are detected by four 1550-nm-optimized WSi superconducting nanowire detectors from NASA's Jet Propulsion Laboratory, with efficiency approximately 80% [41]; Bob's detector B2 had an efficiency of approximately 40% due to coupling fiber misalignment after installation. The outputs of the detectors are collected by a timetagger with 156-ps resolution (UQDevices UQD-Logic-16). The symmetric heralding efficiency into single-mode fiber is approximately 0.01, when including the above detection efficiency, analysis and detection system transmission (approximately 0.3), and entangled-photon-source collection efficiency into single-mode fiber (approximately 0.13).

APPENDIX B: TIME-BIN PHASE STABILIZATION

Due to environmental disturbances, temperature fluctuations, and the simulated Doppler shift, it is necessary to implement an active phase-stabilization system to simultaneously stabilize the phases between $|t_1\rangle$ and $|t_2\rangle$ in both Alice and Charles' and Bob's analyzer interferometers, relative to the pump interferometer. We direct some of the pump light, exiting the unused port of the pump delay interferometer, into the analyzer interferometers (see Fig. 2). The pump light is vertically displaced from the

810-nm photons so it would not propagate through the liquid crystals and receive a phase shift. The light is detected by D_1 and D_2 , low-bandwidth, amplified Si photodiodes (Thorlabs PDA36A), at both output ports of each interferometer. An error signal is calculated from the photodiodes:

$$E \equiv \frac{(I_{D_1} - \gamma I_{D_2})}{(I_{D_1} + \gamma I_{D_2})}, \text{ with } \gamma \approx 0.6. \quad (\text{B1})$$

The factor γ is necessary to balance the different visibilities measured in each output port, since the optics used in the analyzer are designed for the down-conversion wavelengths and not the stabilization wavelength. For each analyzer interferometer, this error signal is input to a proportional-integral (PI) feedback algorithm with a set point of zero and an output rate of 100 Hz. The PI algorithm output is fed to a driver to actuate a piezoelectric crystal on the translation stage of the right-angle prism inside the corresponding analyzer interferometer.

APPENDIX C: TIME-BIN FILTERING

None of the the detectors used in this experiment are gated internally, allowing photon detection at any time. Initially, this presented a problem because there are three pulses emitted from Alice and Charles' and Bob's analyzer interferometers. For this experiment, it is necessary to implement a circuit to filter out events from the outer two pulses, because only the middle pulse contained events with a superposition of time bins. Each pulse emitted from the interferometer has a fixed delay with respect to the input pulse, so employing an AND gate between each detector and the laser clock (with an adjustable delay) created a time filter with a width of approximately 1 ns centered around the middle pulse [17].

APPENDIX D: TOMOGRAPHIC RECONSTRUCTION

To reconstruct the state of the photons received by Bob, 36 different measurements are made by rotating the waveplates, moving the removable polarizer (some settings required a certain polarizer; see Table II), and recording the coincidences between Alice and Bob's detectors.

The measurements performed using the setup in Fig. 8 are

$$\begin{aligned} & \{|H\rangle, |V\rangle, |D\rangle, |A\rangle, |R\rangle, |L\rangle\} \otimes \{|t_1\rangle, |t_2\rangle\} \\ & \{|H\rangle, |V\rangle\} \otimes \left\{ \frac{1}{\sqrt{2}}(|t_1\rangle \pm i|t_2\rangle), \frac{1}{\sqrt{2}}(|t_1\rangle \pm |t_2\rangle) \right\} \end{aligned}$$

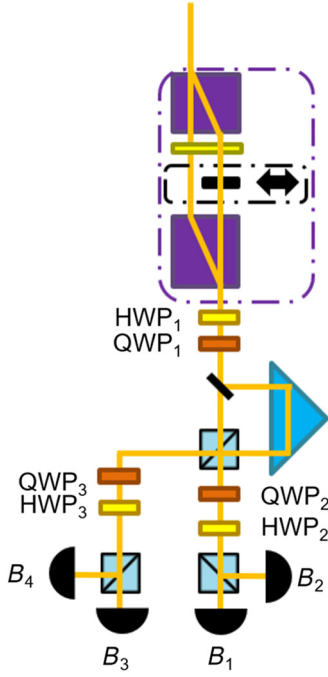


FIG. 8. Tomography system. This schematic shows in more detail the tomography system used to measure Bob's photon.

$$\left\{ \frac{1}{\sqrt{2}}(|Dt_1\rangle \pm i|At_2\rangle), \frac{1}{\sqrt{2}}(|Dt_1\rangle \pm |At_2\rangle), \right. \\ \left. \frac{1}{\sqrt{2}}(|At_1\rangle \pm i|Dt_2\rangle), \frac{1}{\sqrt{2}}(|At_1\rangle \pm |Dt_2\rangle) \right\} \\ \left\{ \frac{1}{\sqrt{2}}(|Rt_1\rangle \pm i|Lt_2\rangle), \frac{1}{\sqrt{2}}(|Rt_1\rangle \pm |Lt_2\rangle), \right. \\ \left. \frac{1}{\sqrt{2}}(|Lt_1\rangle \pm i|Rt_2\rangle), \frac{1}{\sqrt{2}}(|Lt_1\rangle \pm |Rt_2\rangle) \right\}, \quad (\text{D1})$$

where $D(A)$ is (anti)diagonal polarization and $R(L)$ is right(left) circular polarization. These measurements form an informationally overcomplete set in the space of interest; after data collection, they are analyzed to produce four density matrices (one for each tomography conditional on which of Alice's detectors fired) using maximum-likelihood estimation [32].

To measure states in the first group of measurements in Eq. (D1), HWP₂ and HWP₃ are rotated to 0° or 45° to project the detectors onto one time bin or the other but not superpositions of them. HWP₁ and quarter-wave plate QWP₁ in front of the interferometer are used to change what basis the PBS in the interferometer projects on to. To measure states in the second group, the beam block in the removable polarizer moves to block the orthogonal polarization. The polarization is rotated into the D/A basis and HWP₂ and HWP₃ are rotated to 22.5°, so the detectors project onto superpositions of the time bins. Also, to maintain the same level of phase sensitivity across all

measurements, the count time is doubled since the polarizer blocks roughly half the photons. For measurements of the third and fourth groups, HWP₁ and QWP₁ are rotated to put the PBS in the correct basis and HWP₂ and HWP₃ are rotated to 22.5° as before. To change the phase shift between $|t_1\rangle$ and $|t_2\rangle$, QWP₂ and QWP₃ are rotated. See Table II for exact settings.

1. Tomography measurement efficiency calibration

There are four tomographies measured simultaneously, each conditional on one of Alice's four detectors. Additionally, there are four different simultaneous measurements because all four of Bob's detectors projected onto a different state during the nine different settings for the wave plates and polarizer. To allow the use of all four of Bob's detectors for a single tomography, a measurement efficiency calibration is made periodically so the differences in the path and detection efficiencies for B_2 – B_4 could be normalized to Bob's detector B_1 . We calibrate the measurement efficiency of every measurement in the tomography with respect to detector B_1 . This calibration consisted of five tomographies with 36 measurement settings. From these tomographies, we are able to calculate the average measurement efficiency ratio between taking the measurement with detector B_1 and one of the other three detectors (see the four right-most columns of Table I). Table I shows the exact mapping between the states measured in the 9- and 36-setting tomographies. A complete efficiency calibration of Bob's and Alice's measurement systems is not carried out throughout the experiment. Therefore, all tomographies measured include effects from the measurement efficiencies (from the different paths) to Bob's detector B_1 (B_2 – B_4 are normalized to B_1) and the measurement efficiencies for Alice's detectors. We are able to reduce adverse effects on the measured fidelity to approximately 1% by balancing the measurement efficiencies using detector alignment and by adjusting the relative probabilities for the terms in our equimodular state. Without this balancing, the fidelities would have been degraded by approximately 5% to approximately 10%. Effectively, the states that result from our tomography are the states collected by our detectors, not the states that enter our measurement system. Equivalent results would have been obtained for the reconstruction of states that enter our measurement system if a complete system efficiency calibration had been carried out so that the differing path efficiencies could be normalized away and the state creation elements are rebalanced accordingly.

2. MLE optical system representation

For maximum-likelihood state estimation, the optical system is simulated using Jones calculus and is operated on a density matrix with optimizable parameters [32]. The density matrix, ρ_{test} , is constrained to represent a physical

TABLE I. Tomography states. This table details the states that each single-photon detector is projecting onto for each setting of the tomography. Additionally, for the nine-setting tomography, it shows which coincidences are used to calibrate the relative efficiencies of Bob's four detectors for each tomography measurement. For example, C_{S2B1} corresponds to the coincidences with Bob's detector 1 on measurement setting 2 with one of Alice's detectors.

B_1 State	B_2 State	B_3 State	B_4 State	36-sett no.	9-sett np.	B_1 Eff. Cor.	B_2 Eff. Cor.	B_3 Eff. Cor.	B_4 Eff. Cor.
$ H\rangle \frac{1}{\sqrt{2}}(t_1\rangle + t_2\rangle)$	$ H\rangle \frac{1}{\sqrt{2}}(t_1\rangle - t_2\rangle)$	$ H\rangle \frac{1}{\sqrt{2}}(t_1\rangle + i t_2\rangle)$	$ H\rangle \frac{1}{\sqrt{2}}(t_1\rangle - i t_2\rangle)$	1	1	C_{S1B1}/C_{S1B1}	C_{S2B1}/C_{S1B2}	C_{S3B1}/C_{S1B3}	C_{S4B1}/C_{S1B4}
$ H\rangle \frac{1}{\sqrt{2}}(t_1\rangle - t_2\rangle)$	$ H\rangle \frac{1}{\sqrt{2}}(t_1\rangle + t_2\rangle)$	$ H\rangle \frac{1}{\sqrt{2}}(t_1\rangle - i t_2\rangle)$	$ H\rangle \frac{1}{\sqrt{2}}(t_1\rangle + i t_2\rangle)$	2					
$ H\rangle \frac{1}{\sqrt{2}}(t_1\rangle + i t_2\rangle)$	$ H\rangle \frac{1}{\sqrt{2}}(t_1\rangle - i t_2\rangle)$	$ H\rangle \frac{1}{\sqrt{2}}(t_1\rangle + t_2\rangle)$	$ H\rangle \frac{1}{\sqrt{2}}(t_1\rangle - t_2\rangle)$	3					
$ H\rangle \frac{1}{\sqrt{2}}(t_1\rangle - i t_2\rangle)$	$ H\rangle \frac{1}{\sqrt{2}}(t_1\rangle + i t_2\rangle)$	$ H\rangle \frac{1}{\sqrt{2}}(t_1\rangle - t_2\rangle)$	$ H\rangle \frac{1}{\sqrt{2}}(t_1\rangle + t_2\rangle)$	4					
$ V\rangle \frac{1}{\sqrt{2}}(t_1\rangle + t_2\rangle)$	$ V\rangle \frac{1}{\sqrt{2}}(t_1\rangle - t_2\rangle)$	$ V\rangle \frac{1}{\sqrt{2}}(t_1\rangle + i t_2\rangle)$	$ V\rangle \frac{1}{\sqrt{2}}(t_1\rangle - i t_2\rangle)$	5	2	C_{S5B1}/C_{S5B1}	C_{S6B1}/C_{S5B2}	C_{S7B1}/C_{S5B3}	C_{S8B1}/C_{S5B4}
$ V\rangle \frac{1}{\sqrt{2}}(t_1\rangle - t_2\rangle)$	$ V\rangle \frac{1}{\sqrt{2}}(t_1\rangle + t_2\rangle)$	$ V\rangle \frac{1}{\sqrt{2}}(t_1\rangle - i t_2\rangle)$	$ V\rangle \frac{1}{\sqrt{2}}(t_1\rangle + i t_2\rangle)$	6					
$ V\rangle \frac{1}{\sqrt{2}}(t_1\rangle + i t_2\rangle)$	$ V\rangle \frac{1}{\sqrt{2}}(t_1\rangle - i t_2\rangle)$	$ V\rangle \frac{1}{\sqrt{2}}(t_1\rangle + t_2\rangle)$	$ V\rangle \frac{1}{\sqrt{2}}(t_1\rangle - t_2\rangle)$	7					
$ V\rangle \frac{1}{\sqrt{2}}(t_1\rangle - i t_2\rangle)$	$ V\rangle \frac{1}{\sqrt{2}}(t_1\rangle + i t_2\rangle)$	$ V\rangle \frac{1}{\sqrt{2}}(t_1\rangle - t_2\rangle)$	$ V\rangle \frac{1}{\sqrt{2}}(t_1\rangle + t_2\rangle)$	8					
$\frac{1}{\sqrt{2}}(L t_1\rangle + R t_2\rangle)$	$\frac{1}{\sqrt{2}}(L t_1\rangle - R t_2\rangle)$	$\frac{1}{\sqrt{2}}(R t_1\rangle + L t_2\rangle)$	$\frac{1}{\sqrt{2}}(R t_1\rangle - L t_2\rangle)$	9					
$\frac{1}{\sqrt{2}}(L t_1\rangle - R t_2\rangle)$	$\frac{1}{\sqrt{2}}(L t_1\rangle + R t_2\rangle)$	$\frac{1}{\sqrt{2}}(R t_1\rangle - L t_2\rangle)$	$\frac{1}{\sqrt{2}}(R t_1\rangle + L t_2\rangle)$	10					
$\frac{1}{\sqrt{2}}(L t_1\rangle + i R t_2\rangle)$	$\frac{1}{\sqrt{2}}(L t_1\rangle - i R t_2\rangle)$	$\frac{1}{\sqrt{2}}(R t_1\rangle + i L t_2\rangle)$	$\frac{1}{\sqrt{2}}(R t_1\rangle - i L t_2\rangle)$	11					
$\frac{1}{\sqrt{2}}(L t_1\rangle - i R t_2\rangle)$	$\frac{1}{\sqrt{2}}(L t_1\rangle + i R t_2\rangle)$	$\frac{1}{\sqrt{2}}(R t_1\rangle - i L t_2\rangle)$	$\frac{1}{\sqrt{2}}(R t_1\rangle + i L t_2\rangle)$	12					
$\frac{1}{\sqrt{2}}(L t_1\rangle - R t_2\rangle)$	$\frac{1}{\sqrt{2}}(L t_1\rangle + R t_2\rangle)$	$\frac{1}{\sqrt{2}}(R t_1\rangle - L t_2\rangle)$	$\frac{1}{\sqrt{2}}(R t_1\rangle + L t_2\rangle)$	13	3	C_{S13B1}/C_{S13B1}	C_{S14B1}/C_{S13B2}	C_{S17B1}/C_{S13B3}	C_{S18B1}/C_{S13B4}
$\frac{1}{\sqrt{2}}(D t_1\rangle + A t_2\rangle)$	$\frac{1}{\sqrt{2}}(D t_1\rangle - A t_2\rangle)$	$\frac{1}{\sqrt{2}}(D t_1\rangle - A t_2\rangle)$	$\frac{1}{\sqrt{2}}(D t_1\rangle + A t_2\rangle)$	14					
$\frac{1}{\sqrt{2}}(D t_1\rangle - A t_2\rangle)$	$\frac{1}{\sqrt{2}}(D t_1\rangle + A t_2\rangle)$	$\frac{1}{\sqrt{2}}(D t_1\rangle + A t_2\rangle)$	$\frac{1}{\sqrt{2}}(D t_1\rangle - A t_2\rangle)$	15	4	C_{S15B1}/C_{S15B1}	C_{S16B1}/C_{S15B2}	C_{S19B1}/C_{S15B3}	C_{S20B1}/C_{S15B4}
$\frac{1}{\sqrt{2}}(D t_1\rangle + i A t_2\rangle)$	$\frac{1}{\sqrt{2}}(D t_1\rangle - i A t_2\rangle)$	$\frac{1}{\sqrt{2}}(D t_1\rangle + i A t_2\rangle)$	$\frac{1}{\sqrt{2}}(D t_1\rangle - i A t_2\rangle)$	16					
$\frac{1}{\sqrt{2}}(A t_1\rangle + D t_2\rangle)$	$\frac{1}{\sqrt{2}}(A t_1\rangle - D t_2\rangle)$	$\frac{1}{\sqrt{2}}(D t_1\rangle + A t_2\rangle)$	$\frac{1}{\sqrt{2}}(D t_1\rangle - A t_2\rangle)$	17					
$\frac{1}{\sqrt{2}}(A t_1\rangle - D t_2\rangle)$	$\frac{1}{\sqrt{2}}(A t_1\rangle + D t_2\rangle)$	$\frac{1}{\sqrt{2}}(D t_1\rangle - A t_2\rangle)$	$\frac{1}{\sqrt{2}}(D t_1\rangle + A t_2\rangle)$	18					
$\frac{1}{\sqrt{2}}(A t_1\rangle + i D t_2\rangle)$	$\frac{1}{\sqrt{2}}(A t_1\rangle - i D t_2\rangle)$	$\frac{1}{\sqrt{2}}(D t_1\rangle + i A t_2\rangle)$	$\frac{1}{\sqrt{2}}(D t_1\rangle - i A t_2\rangle)$	19					
$\frac{1}{\sqrt{2}}(A t_1\rangle - i D t_2\rangle)$	$\frac{1}{\sqrt{2}}(A t_1\rangle + i D t_2\rangle)$	$\frac{1}{\sqrt{2}}(D t_1\rangle - i A t_2\rangle)$	$\frac{1}{\sqrt{2}}(D t_1\rangle + i A t_2\rangle)$	20					
$\frac{1}{\sqrt{2}}(R t_1\rangle + L t_2\rangle)$	$\frac{1}{\sqrt{2}}(R t_1\rangle - L t_2\rangle)$	$\frac{1}{\sqrt{2}}(R t_1\rangle + L t_2\rangle)$	$\frac{1}{\sqrt{2}}(R t_1\rangle - L t_2\rangle)$	21	5	C_{S21B1}/C_{S21B1}	C_{S22B1}/C_{S21B2}	C_{S25B1}/C_{S21B3}	C_{S26B1}/C_{S21B4}
$\frac{1}{\sqrt{2}}(R t_1\rangle - L t_2\rangle)$	$\frac{1}{\sqrt{2}}(R t_1\rangle + L t_2\rangle)$	$\frac{1}{\sqrt{2}}(R t_1\rangle - L t_2\rangle)$	$\frac{1}{\sqrt{2}}(R t_1\rangle + L t_2\rangle)$	22					
$\frac{1}{\sqrt{2}}(R t_1\rangle + i L t_2\rangle)$	$\frac{1}{\sqrt{2}}(R t_1\rangle - i L t_2\rangle)$	$\frac{1}{\sqrt{2}}(R t_1\rangle + i L t_2\rangle)$	$\frac{1}{\sqrt{2}}(R t_1\rangle - i L t_2\rangle)$	23	6	C_{S23B1}/C_{S23B1}	C_{S24B1}/C_{S23B2}	C_{S27B1}/C_{S23B3}	C_{S28B1}/C_{S23B4}
$\frac{1}{\sqrt{2}}(R t_1\rangle - i L t_2\rangle)$	$\frac{1}{\sqrt{2}}(R t_1\rangle + i L t_2\rangle)$	$\frac{1}{\sqrt{2}}(R t_1\rangle - i L t_2\rangle)$	$\frac{1}{\sqrt{2}}(R t_1\rangle + i L t_2\rangle)$	24					
$ A t_1\rangle$	$ D t_2\rangle$	$ A t_2\rangle$	$ D t_1\rangle$	25					
$ H t_1\rangle$	$ V t_2\rangle$	$ H t_2\rangle$	$ V t_1\rangle$	26	7	C_{S26B1}/C_{S26B1}	C_{S27B1}/C_{S26B2}	C_{S30B1}/C_{S26B3}	C_{S31B1}/C_{S26B4}
$ L t_1\rangle$	$ R t_2\rangle$	$ L t_2\rangle$	$ R t_1\rangle$	27					
$ V t_1\rangle$	$ H t_2\rangle$	$ V t_2\rangle$	$ H t_1\rangle$	28					
$ D t_1\rangle$	$ A t_2\rangle$	$ D t_2\rangle$	$ A t_1\rangle$	29	8	C_{S29B1}/C_{S29B1}	C_{S30B1}/C_{S29B2}	C_{S33B1}/C_{S29B3}	C_{S34B1}/C_{S29B4}
$ R t_1\rangle$	$ L t_2\rangle$	$ R t_2\rangle$	$ L t_1\rangle$	30	9	C_{S30B1}/C_{S30B1}	C_{S31B1}/C_{S30B2}	C_{S34B1}/C_{S30B3}	C_{S35B1}/C_{S30B4}
$ D t_2\rangle$	$ A t_1\rangle$	$ D t_1\rangle$	$ A t_2\rangle$	31					
$ V t_2\rangle$	$ H t_1\rangle$	$ V t_1\rangle$	$ H t_2\rangle$	32					
$ R t_2\rangle$	$ L t_1\rangle$	$ R t_1\rangle$	$ L t_2\rangle$	33					
$ H t_2\rangle$	$ V t_1\rangle$	$ H t_1\rangle$	$ V t_2\rangle$	34					
$ A t_2\rangle$	$ D t_1\rangle$	$ A t_1\rangle$	$ D t_2\rangle$	35					
$ L t_2\rangle$	$ R t_1\rangle$	$ L t_1\rangle$	$ R t_2\rangle$	36					

state using a Cholesky decomposition:

$$\rho_{\text{test}} = U_{\text{test}} \times L_{\text{test}}, \quad (\text{D2})$$

where

$$L_{\text{test}} \equiv \begin{bmatrix} t_1 & 0 & 0 & 0 \\ t_5 + it_6 & t_2 & 0 & 0 \\ t_7 + it_8 & t_{11} + it_{12} & t_3 & 0 \\ t_9 + it_{10} & t_{13} + it_{14} & t_{15} + it_{16} & t_4 \end{bmatrix} \text{ and}$$

$$U_{\text{test}} \equiv \begin{bmatrix} t_1 & t_5 - it_6 & t_7 - it_8 & t_9 - it_{10} \\ 0 & t_2 & t_{11} - it_{12} & t_{13} - it_{14} \\ 0 & 0 & t_3 & t_{15} - it_{16} \\ 0 & 0 & 0 & t_4 \end{bmatrix}. \quad (\text{D3})$$

We represent the optical system making the measurement as

$$\text{Measp}_i \equiv \text{Setang}_i \times \text{Setang}_i^\dagger, \quad (\text{D4})$$

where Setang_i is the quantum state for that combination of measurement settings.

$$\text{Setang}_1 \equiv P_r \times H_1 \times Q_1 \times M$$

$$\times \text{Interf}_{P_1} \times Q_2 \times H_2 \times \begin{bmatrix} 1 \\ 0 \end{bmatrix}, \quad (\text{D5})$$

$$\text{Setang}_2 \equiv P_r \times H_1 \times Q_1 \times M$$

$$\times \text{Interf}_{P_1} \times Q_2 \times \text{HWP}_2 \times \begin{bmatrix} 0 \\ 1 \end{bmatrix}, \quad (\text{D6})$$

$$\text{Setang}_3 \equiv P_r \times H_1 \times Q_1 \times M$$

$$\times \text{Interf}_{P_2} \times Q_3 \times H_3 \times \begin{bmatrix} 1 \\ 0 \end{bmatrix}, \quad (\text{D7})$$

$$\text{Setang}_4 \equiv P_r \times H_1 \times Q_1 \times M$$

$$\times \text{Interf}_{P_2} \times Q_3 \times H_3 \times \begin{bmatrix} 0 \\ 1 \end{bmatrix}, \quad (\text{D8})$$

$$\text{Interf}_{P_1} \equiv \begin{bmatrix} 1 & 0 \\ 0 & 0 \\ 0 & 0 \\ 0 & 1 \end{bmatrix}, \quad (\text{D9})$$

$$\text{Interf}_{P_2} \equiv \begin{bmatrix} 0 & 0 \\ 1 & 0 \\ 0 & 1 \\ 0 & 0 \end{bmatrix}, \quad (\text{D10})$$

$$M \equiv \begin{bmatrix} 1 & 0 & 0 & 0 \\ 0 & -1 & 0 & 0 \\ 0 & 0 & 1 & 0 \\ 0 & 0 & 0 & -1 \end{bmatrix}, \quad (\text{D11})$$

$$P_r \equiv \begin{bmatrix} (2T_H - T_V)T_H & 0 & 0 & 0 \\ 0 & (2T_V - T_H)T_V & 0 & 0 \\ 0 & 0 & (2T_H - T_V)T_H & 0 \\ 0 & 0 & 0 & (2T_V - T_H)T_V \end{bmatrix}, \quad (\text{D12})$$

$$H_1 \equiv \begin{bmatrix} \cos(2\alpha_1) & -2\cos(\alpha_1)\sin(\alpha_1) & 0 & 0 \\ -2\cos(\alpha_1)\sin(\alpha_1) & -\cos(2\alpha_1) & 0 & 0 \\ 0 & 0 & \cos(2\alpha_1) & -2\cos(\alpha_1)\sin(\alpha_1) \\ 0 & 0 & -2\cos(\alpha_1)\sin(\alpha_1) & -\cos(2\alpha_1) \end{bmatrix}, \quad (\text{D13})$$

$$Q_1 \equiv \begin{bmatrix} \cos^2(\beta_1) + i\sin^2(\beta_1) & (i-1)\cos(\beta_1)\sin(\beta_1) & 0 & 0 \\ (i-1)\cos(\beta_1)\sin(\beta_1) & i\cos^2(\beta_1) + \sin^2(\beta_1) & 0 & 0 \\ 0 & 0 & \cos^2(\beta_1) + i\sin^2(\beta_1) & (i-1)\cos(\beta_1)\sin(\beta_1) \\ 0 & 0 & (i-1)\cos(\beta_1)\sin(\beta_1) & i\cos^2(\beta_1) + \sin^2(\beta_1) \end{bmatrix}, \quad (\text{D14})$$

$$H_j \equiv \begin{bmatrix} \cos(2\alpha_j) & -2\cos(\alpha_j)\sin(\alpha_j) \\ -2\cos(\alpha_j)\sin(\alpha_j) & -\cos(2\alpha_j) \end{bmatrix} \text{ for } j \equiv \{2, 3\}, \quad (\text{D15})$$

$$Q_j \equiv \begin{bmatrix} \cos^2(\beta_j) + i \sin^2(\beta_j) & (i-1) \cos(\beta_j) \sin(\beta_j) \\ (i-1) \cos(\beta_j) \sin(\beta_j) & i \cos^2(\beta_j) + \sin^2(\beta_j) \end{bmatrix} \\ \times \text{ for } j = \{2, 3\}, \quad (\text{D16})$$

where Interf_{P1} , Interf_{P2} , M , P_r , H_1 , Q_1 , H_j , Q_j represent optical operations from port 1 of the interferometer, port 2 of the interferometer, flipping perspective from projector to source, removable polarizer, HWP in before the interferometer, QWP before the interferometer, HWPs after the interferometer, and QWPs after the interferometer. $\alpha_1, \alpha_2, \alpha_3$ are the angles of half-wave plates 1–3, and $\beta_1, \beta_2, \beta_3$ are the angles of quarter-wave plates 1–3. T_H and T_V are the transmission settings of the removable polarizer; for example, if $T_H = 1$ and $T_V = 0$, the removable polarizer is positioned such that $|H\rangle$ is transmitted while $|V\rangle$ is

blocked. The angles and positions of these elements during a tomography are listed in Table II.

3. Representative data and error analysis

The real parts of the density matrices of the expected and received states for a typical superdense teleported state are shown in Fig. 9. The received states are reconstructed from the data in Table III. This data is taken while counting for 15 s for each setting, except the settings that use the movable polarizer in front of Bob's interferometer (9 settings no. 1-2, 36 settings no. 1-8), which use a count time of 30 s. The pump power is approximately 0.5 mW at the PPLN crystal.

From measurements of components in our system and detailed numerical simulation, we find approximately 1%

TABLE II. Tomography settings. This table details the angles of the wave plates and positions of the polarizers for each setting of the tomography. $\alpha_1, \alpha_2, \alpha_3$ are the angles of half-wave plates 1–3; similarly $\beta_1, \beta_2, \beta_3$ are the angles of quarter-wave plates 1–3. T_H and T_V are transmission settings of the removable polarizer.

α_1	β_1	α_2	β_2	α_3	β_3	T_H	T_V	36 settings no.	9 settings no.
22.5	0	−22.5	0	−22.5	45	1	0	1	1
22.5	0	22.5	0	22.5	45	1	0	2	
22.5	0	22.5	45	−22.5	0	1	0	3	
22.5	0	−22.5	45	22.5	0	1	0	4	
67.5	0	−22.5	0	−22.5	45	1	0	5	2
67.5	0	22.5	0	22.5	45	1	0	6	
67.5	0	22.5	45	−22.5	0	1	0	7	
67.5	0	−22.5	45	22.5	0	1	0	8	
0	−45	−22.5	0	−22.5	0	1	1	9	
0	−45	22.5	0	22.5	0	1	1	10	
0	−45	−22.5	45	22.5	45	1	1	11	
0	−45	22.5	45	−22.5	45	1	1	12	
22.5	0	−22.5	0	−22.5	0	1	1	13	3
22.5	0	22.5	0	22.5	0	1	1	14	
22.5	0	22.5	45	−22.5	45	1	1	15	4
22.5	0	−22.5	45	22.5	45	1	1	16	
−22.5	0	22.5	0	22.5	0	1	1	17	
−22.5	0	−22.5	0	−22.5	0	1	1	18	
−22.5	0	−22.5	45	22.5	45	1	1	19	
−22.5	0	22.5	45	−22.5	45	1	1	20	
0	45	22.5	0	22.5	0	1	1	21	5
0	45	−22.5	0	−22.5	0	1	1	22	
0	45	22.5	45	−22.5	45	1	1	23	6
0	45	−22.5	45	22.5	45	1	1	24	
−22.5	0	0	0	0	0	1	1	25	
0	0	0	0	0	0	1	1	26	7
0	−45	0	0	0	0	1	1	27	
45	0	0	0	0	0	1	1	28	
22.5	0	0	0	0	0	1	1	29	8
0	45	0	0	0	0	1	1	30	9
−22.5	0	45	0	45	0	1	1	31	
0	0	45	0	45	0	1	1	32	
0	−45	45	0	45	0	1	1	33	
45	0	45	0	45	0	1	1	34	
22.5	0	45	0	45	0	1	1	35	
0	45	45	0	45	0	1	1	36	

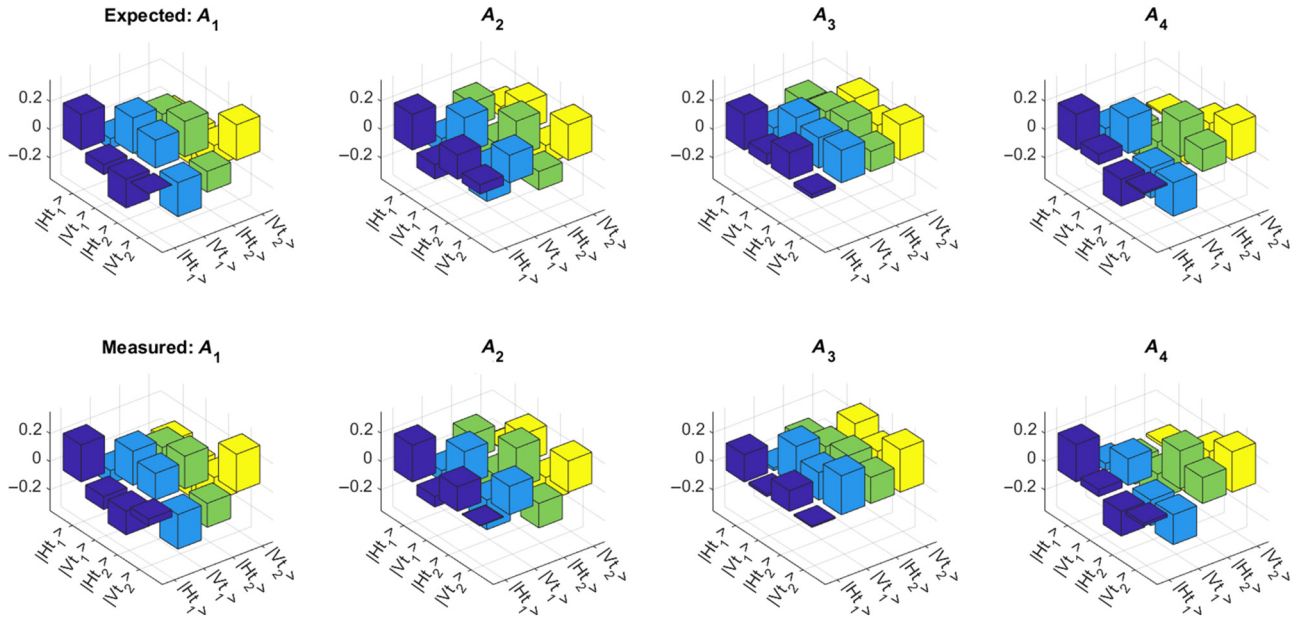


FIG. 9. Representative density matrix. Real part of expected and reconstructed density matrices for the states received by Bob, labeled by Alice's measurement outcome. The raw counts data is shown in Table III. Fidelities between measured and expected states for A_1, A_2, A_3 , and A_4 are 0.94, 0.93, 0.95, and 0.94, respectively.

drop in fidelity from imperfect polarizer extinction ratios, approximately 1% from imperfect LC basis and phase settings, approximately 1% from unbalanced measurement

efficiencies, approximately 1% from imperfect time-bin qubit purity, and approximately 2% from imperfect H/V and D/A visibility in the removable polarizer.

TABLE III. Representative tomography data. The singles and coincidence counts measured for each setting in a tomography (the columns) for one of the states measured in Fig. 4, specifically the state in Fig. 9.

	S_1	S_2	S_3	S_4	S_5	S_6	S_7	S_8	S_9
B_1	29949	25686	26331	25949	25191	25012	25652	23395	23406
B_2	12941	10932	11038	10498	10700	10119	9661	10734	10380
B_3	27435	23110	23143	23160	23173	22491	27544	25522	24393
B_4	24420	20883	22465	22911	22642	22363	19845	21442	20850
A_1	86564	86551	43178	43346	43569	43402	43130	42959	43427
A_2	105626	105481	53170	53243	53024	52850	52738	52551	52779
A_3	88503	88778	44113	44585	44397	44618	44667	44357	44268
A_4	115955	115985	57990	58466	58221	57844	57752	57605	57662
B_1A_1	193	247	62	20	116	76	126	87	16
B_2A_1	15	2	77	84	26	41	44	79	74
B_3A_1	43	111	67	159	192	216	88	31	41
B_4A_1	155	111	94	30	73	46	103	150	218
B_1A_2	51	13	238	272	69	140	153	89	19
B_2A_2	96	107	39	14	47	37	36	78	80
B_3A_2	277	203	181	47	85	77	143	52	50
B_4A_2	34	70	56	183	165	243	138	163	232
B_1A_3	28	7	53	15	177	67	93	111	224
B_2A_3	63	100	48	52	39	83	53	13	13
B_3A_3	191	139	59	233	85	100	108	205	207
B_4A_3	20	86	212	47	98	79	122	73	9
B_1A_4	302	273	178	226	67	231	185	183	267
B_2A_4	13	4	16	16	75	22	63	14	10
B_3A_4	41	87	215	40	80	87	114	224	236
B_4A_4	173	128	86	239	133	105	104	81	7

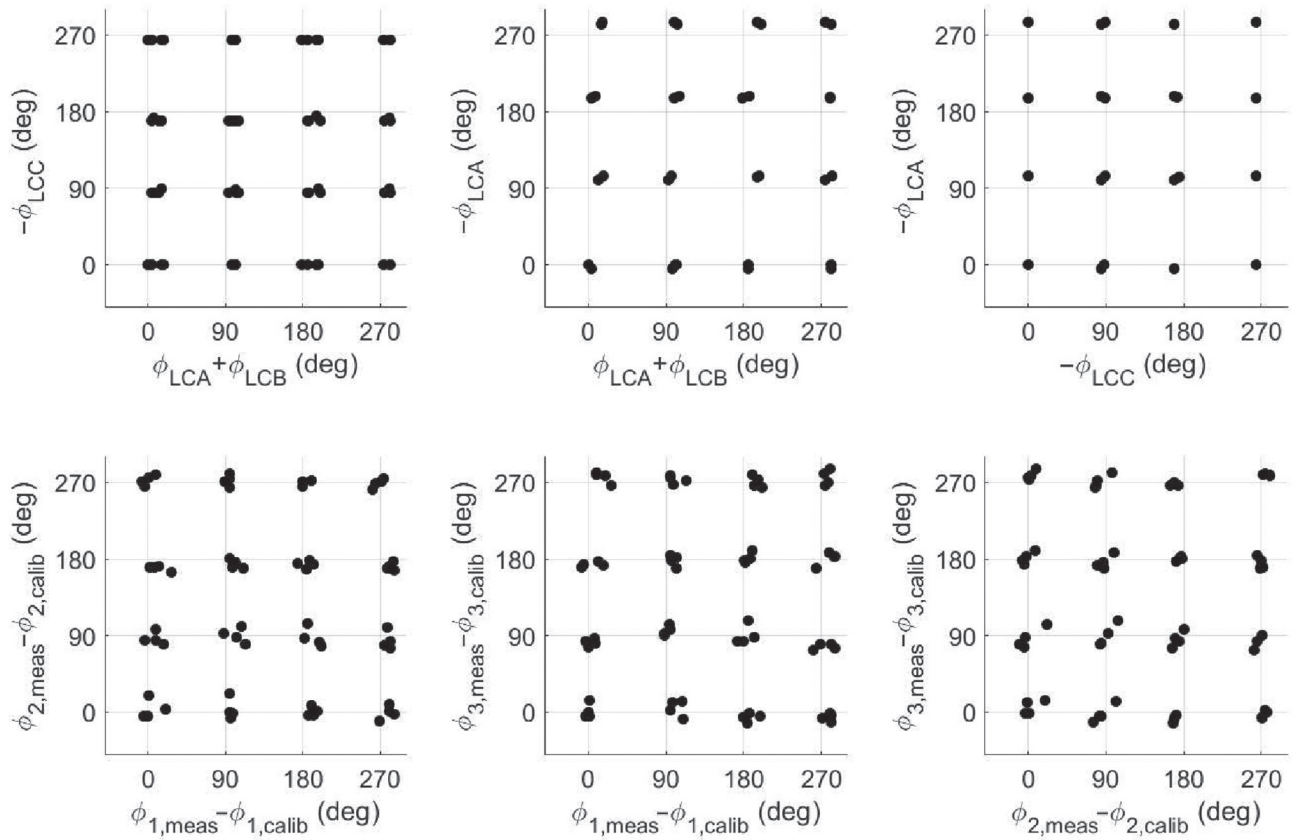


FIG. 10. Projections onto 90° grid. Averaged projections onto 90° grid over eight independent measurements of each grid. (Top row) Target projections based on liquid-crystal phase calibration. (Bottom row) Measured phase projections after subtracting calibrated phase offset.

4. Full state tomography

To measure the total joint state of the entangled photon pairs, a few additions are made to the system to allow a tomography to be measured on Alice and Charles' photon: a half- and a quarter-wave plate are added before Alice and Charles' interferometer and then a quarter-wave plate

is added to each output port of the interferometer; additionally, a removable polarizer is added before the interferometer. The setup diagram during this measurement is in Fig. 11. The tomography is measured using 36 (Alice's and Charles' settings) $\times 36$ (Bob's settings) = 1296 settings.

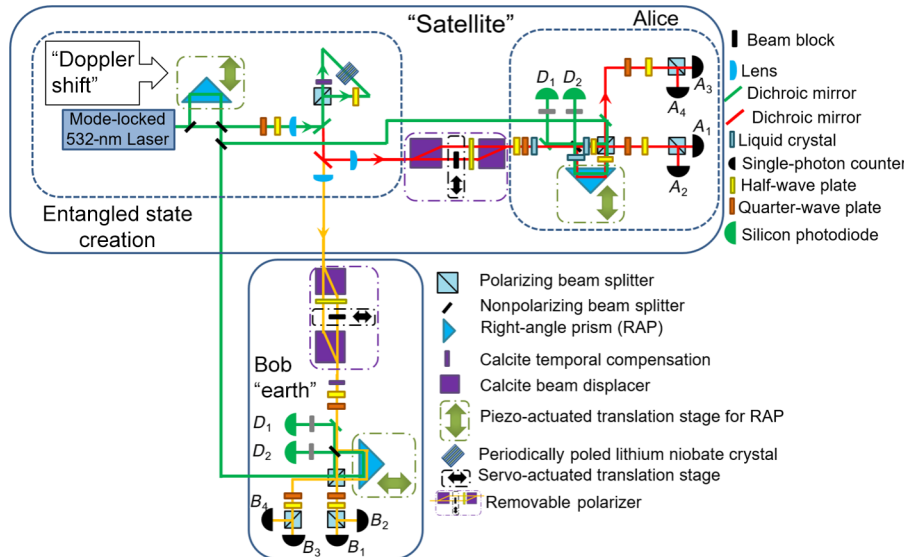


FIG. 11. Full state tomography optical setup. To measure the full state tomography of both photons, several half-wave plates, quarter-wave plates, and a removable polarizer are added to Alice's and Charles' measurement setup to enable the same measurements that are performed on Bob's photon.

APPENDIX E: LIQUID-CRYSTAL CALIBRATION

To calibrate the phase applied by each liquid crystal for each driving voltage, a tomography is measured on Bob's photon (as above) conditioned on detection of Alice's photon by detector A_1 ; the phase between H and V is then extracted from the density matrix. This is distinctly different from the phase extraction used in the analysis of the SDT protocol trials—in that case all phases are extracted, including between the time bins. Here, effectively only a polarization tomography is conducted to measure the phase between H and V applied by the liquid crystal. Additionally, to reduce phase error as much as possible, it is necessary to periodically (approximately 2 days) recalibrate the phase applied by the liquid crystals as measured from the tomography system. Otherwise a drift as much as 20° is observed, due to an induced change in the phase extraction from a varying measurement-efficiency imbalance. The tomography involves many projective measurements, each with a different efficiency, and such differences can modify the extracted phase values.

APPENDIX F: TWO-SAMPLE KS TESTS

In order to assess the resolving power of our system to distinguish states with nearby phase values, for each phase (ϕ_1 , ϕ_2 , and ϕ_3), we create distributions for two closely spaced phase settings (two liquid-crystal settings) of ten

samples each; we then apply a two-sample Kolmogorov-Smirnov test [26] to test the null hypothesis (once for each phase) that all 20 samples are from the same distribution (liquid-crystal setting). The distributions and their empirical cumulative distribution functions (CDF) are shown in Fig. 12. These distributions have a standard deviation of 3° and are, on average, separated by 7° . The two-sample KS test statistic is

$$D_{k,l} = \sup_x |F_{1,k}(x) - F_{2,l}(x)|, \quad (\text{F1})$$

where $F_{1,k}$ and $F_{2,l}$ are the empirical distribution functions of the first and second sample, respectively. The null hypothesis is rejected with a confidence level of α if

$$D_{k,l} > c(\alpha) \sqrt{\frac{k+l}{kl}}, \quad \text{where } c(\alpha) \equiv \sqrt{-\frac{1}{2} \ln\left(\frac{\alpha}{2}\right)}, \quad (\text{F2})$$

and k and l are the number of samples in each distribution. We applied the two-sample KS test to the distributions shown in Fig. 12, concluding that we can reject the null hypothesis that the data are drawn from a single distribution with $\alpha = 0.05$, in other words, with a 5% probability of wrongly rejecting the null hypothesis. We also apply the two-sample KS test to the two distributions shown

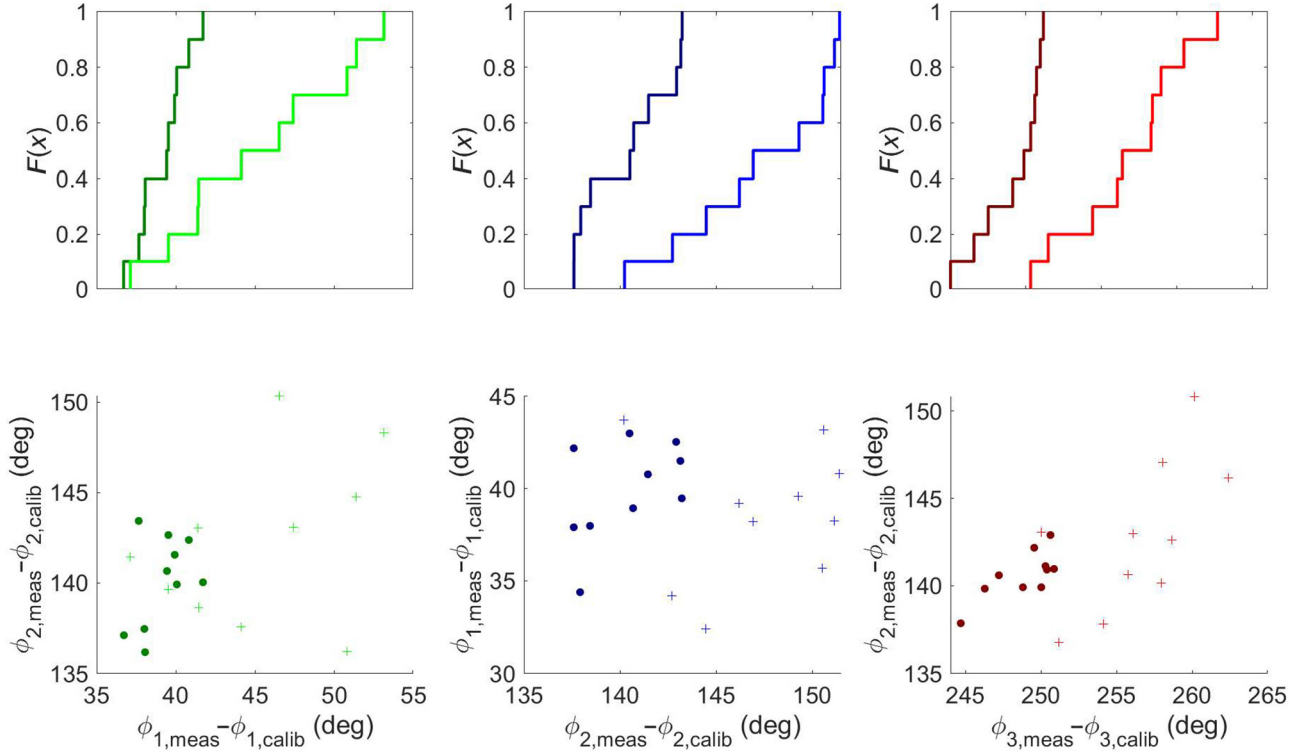


FIG. 12. Two-sample KS tests of very closely spaced distributions in phase space. (Top row) Empirical CDF of phase space data along horizontal axis. (Bottom row) Measured points in phase space. Crosses (dots) are measurements of the (un)displaced distributions. The distributions of crosses (dots) are centered over 45° (39°), 147° (140°), 256° (249°) for ϕ_1 , ϕ_2 , and ϕ_3 , respectively.

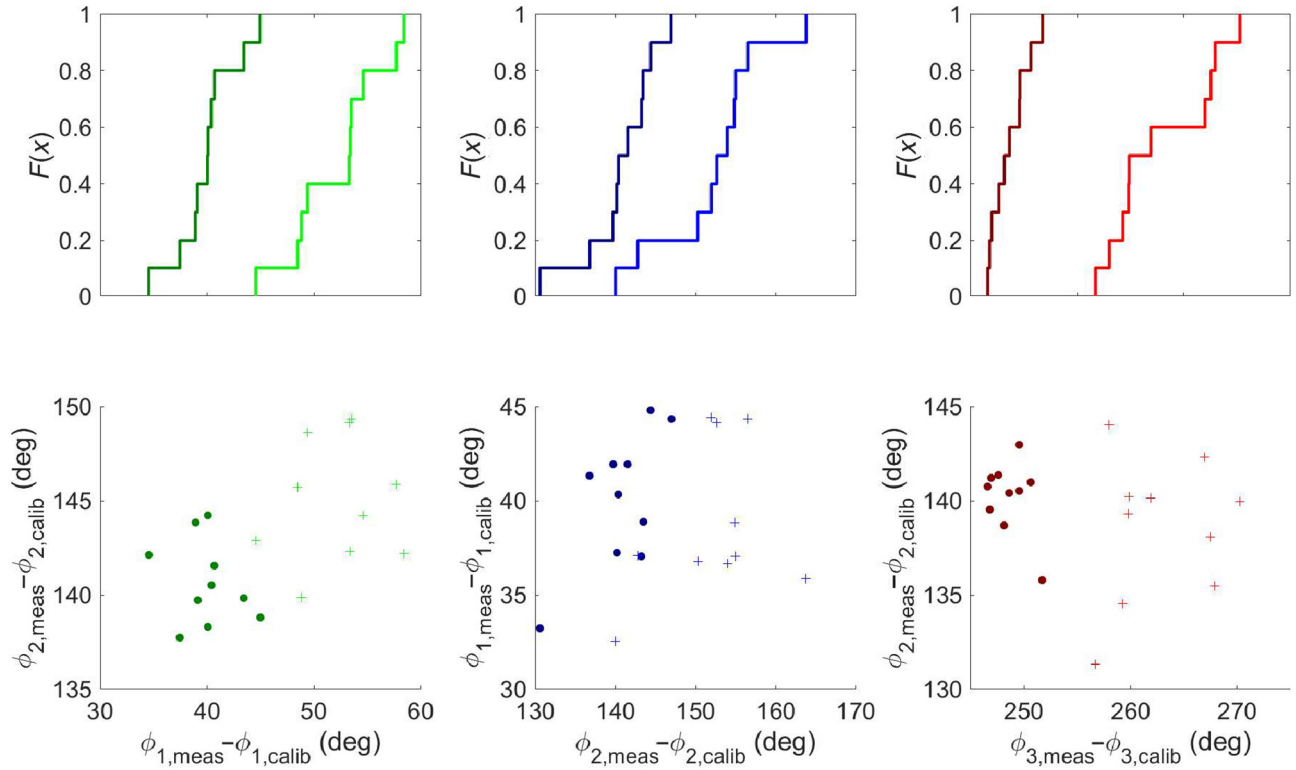


FIG. 13. Two-sample KS tests of moderately closely spaced distributions in phase space. (Top row) Empirical CDF of phase space data along horizontal axis. (Bottom row) Measured points in phase space. Crosses (dots) are measurements of the (un)displaced distributions. The distributions of crosses (dots) are centered over $52^\circ(39^\circ)$, $152^\circ(141^\circ)$, $263^\circ(249^\circ)$ for ϕ_1 , ϕ_2 , and ϕ_3 , respectively.

in Fig. 13; these distributions had a standard deviation of 5° , with means separated by 13° . After applying the two-sample KS test, we reject the null hypothesis that they are the same distribution with $\alpha = 0.005$.

APPENDIX G: DOPPLER SHIFT

The Doppler-effect-induced phase shift is dependent on many orbital parameters, including the elevation angle of the orbit, which changes per pass and is at a maximum for passes directly overhead. Calculations using the relativistic longitudinal Doppler shift equation [42] show an expected

shift (see Fig. 14) of

$$\Delta t(t) = \left[\sqrt{\frac{1 + V_{\text{sat}}(t)/c}{1 - V_{\text{sat}}(t)/c}} - 1 \right] (1.5 \text{ ns}), \quad (\text{G1})$$

assuming time bins separated by 1.5 ns and that the maximum elevation angle during a pass for the orbit of the simulated satellite is about 90° . If acquisition starts and stops at a 20° elevation angle, then the total Δt from t_{start} to t_{stop} is $\Delta t(t_{\text{stop}}) - \Delta t(t_{\text{start}}) = 43 \text{ fs}$ (or $\Delta L = 12.8 \mu\text{m}$).

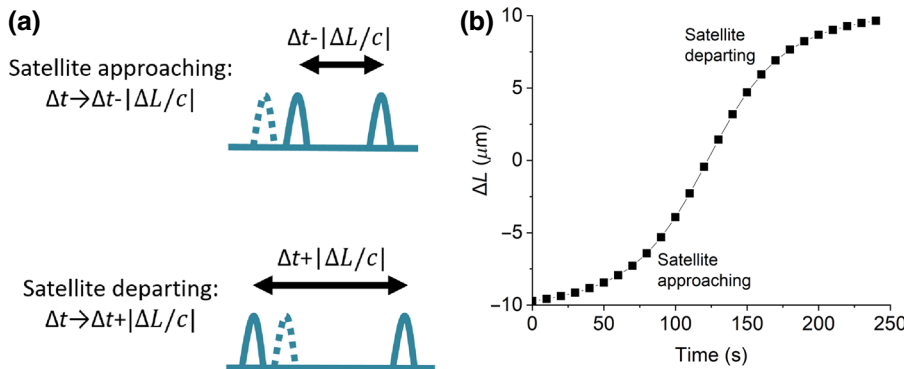


FIG. 14. Expected Doppler shift. (a) Pictorial explanation of the effect of Doppler shift on time bins. (b) Expected Doppler shift for overhead orbit (approximately 90° elevation angle) of satellite with velocity 7.7 km/s.

We implement an in-lab simulation of this Doppler shift, during our compensation system testing, by moving a piezo-actuated translation stage, which controlled the position of the pump's right-angle prism with a distance-versus-time profile matching Eq. (G1), as in Fig. 14. There is also a Doppler shift on the frequency on the photons; however, the frequency shift is negligible since the photon bandwidth is approximately 1 nm and

$$\gamma \equiv \frac{1}{\sqrt{1 - (V_{\text{sat}}/c)^2}} = 1.00000000033, \quad (\text{G2})$$

i.e., quite close to 1 for $V_{\text{sat}} = 7.7$ km/s.

-
- [1] Marcello Caleffi, Angela Sara Cacciapuoti, and Giuseppe Bianchi, in *Proc. of the 5th ACM Int. Conf. on Nano. Comp. and Commun.*, NANOCOM '18 (Association for Computing Machinery, New York, NY, USA, 2018).
 - [2] M. Aspelmeyer, T. Jennewein, M. Pfennigbauer, W. R. Leeb, and A. Zeilinger, Long-distance quantum communication with entangled photons using satellites, *IEEE J. Sel. Top. Q. Elec.* **9**, 1541 (2003).
 - [3] Vittorio Giovannetti, Seth Lloyd, and Lorenzo Maccone, Quantum-enhanced positioning and clock synchronization, *Nature* **412**, 417 (2001).
 - [4] D. Gottesman, T. Jennewein, and S. Croke, Longer-baseline telescopes using quantum repeaters, *IEEE J. Sel. Top. Q. Elec.* **109**, 070503 (2012).
 - [5] Emil T. Khabiboulline, Johannes Borregaard, Kristiaan De Greve, and Mikhail D. Lukin, Optical Interferometry with Quantum Networks, *Phys. Rev. Lett.* **123**, 070504 (2019).
 - [6] Emil T. Khabiboulline, Johannes Borregaard, Kristiaan De Greve, and Mikhail D. Lukin, Quantum-assisted telescope arrays, *Phys. Rev. A* **100**, 022316 (2019).
 - [7] Christoph Simon, Towards a global quantum network, *Nat. Phot.* **11**, 678 (2017).
 - [8] Imran Khan, Bettina Heim, Andreas Neuzner, and Christoph Marquardt, Satellite-based qkd, *Opt. Photon. News* **29**, 26 (2018).
 - [9] Juan Yin *et al.*, Satellite-based entanglement distribution over 1200 kilometers, *Science* **356**, 1140 (2017).
 - [10] Sheng-Kai Liao *et al.*, Satellite-to-ground quantum key distribution, *Nature* **549**, 43 (2017).
 - [11] Sheng-Kai Liao, Wen-Qi Cai, Johannes Handsteiner, Bo Liu, Juan Yin, Liang Zhang, Dominik Rauch, Matthias Fink, and Ji-Gang Ren, Satellite-Relayed Intercontinental Quantum Network, *Phys. Rev. Lett.* **120**, 030501 (2018).
 - [12] Ji-Gang Ren *et al.*, Ground-to-satellite quantum teleportation, *Nature* **549**, 70 (2017).
 - [13] James A. Grieve, Robert Bedington, Zhongkan Tang, Rakhitha C. M. R. B. Chandrasekara, and Alexander Ling, Spooqsats: Cubesats to demonstrate quantum key distribution technologies, *Acta Astronaut.* **151**, 103 (2018).
 - [14] Giuseppe Vallone, Davide Bacco, Daniele Dequal, Simone Gaiarin, Vincenza Luceri, Giuseppe Bianco, and Paolo Villoresi, Experimental Satellite Quantum Communications, *Phys. Rev. Lett.* **115**, 040502 (2015).
 - [15] Christopher J. Pugh, Sarah Kaiser, Jean-Philippe Bourgoin, Jeongwan Jin, Nigar Sultana, Sascha Agne, Elena Anisimova, Vadim Makarov, Eric Choi, Brendon L. Higgins, and Thomas Jennewein, Airborne demonstration of a quantum key distribution receiver payload, *Quant. Sci. Tech.* **2**, 024009 (2017).
 - [16] Fabian Steinlechner, Sebastian Ecker, Matthias Fink, Bo Liu, Jessica Bavaresco, Marcus Huber, Thomas Scheidl, and Rupert Ursin, Distribution of high-dimensional entanglement via an intra-city free-space link, *Nat. Commun.* **8**, 15971 (2017).
 - [17] Joseph C. Chapman, Charles C. W. Lim, and Paul G. Kwiat, Hyperentangled time-bin and polarization quantum key distribution, arXiv:1908.09018 (2019).
 - [18] H. Bernstein, Superdense quantum teleportation, *Quant. Info. Process.* **5**, 451 (2006).
 - [19] Christopher K. Zeidler, Joseph C. Chapman, Eric Chitambar, and Paul G. Kwiat, Tests of nonlocality with hyperentangled photons (to be published).
 - [20] Trent M. Graham, Herbert J. Bernstein, Tzu-Chieh Wei, Marius Junge, and Paul G. Kwiat, Superdense teleportation using hyperentangled photons, *Nat. Commun.* **6**, 1 (2015).
 - [21] T. M. Graham, Ph.D. thesis, School University of Illinois at Urbana-Champaign, 2016.
 - [22] A. Broadbent, J. Fitzsimons, and E. Kashefi, in *2009 50th Annual IEEE Symposium on Foundations of Computer Science*, (2009), p. 517.
 - [23] Xi-Lin Wang, Xin-Dong Cai, Zu-En Su, Ming-Cheng Chen, Dian Wu, Li Li, Nai-Le Liu, Chao-Yang Lu, and Jian-Wei Pan, Quantum teleportation of multiple degrees of freedom of a single photon, *Nature* **518**, 516 (2015).
 - [24] Yi-Han Luo, Han-Sen Zhong, Manuel Erhard, Xi-Lin Wang, Li-Chao Peng, Mario Krenn, Xiao Jiang, Li Li, Nai-Le Liu, and Chao-Yang Lu, Quantum Teleportation in High Dimensions, *Phys. Rev. Lett.* **123**, 070505 (2019).
 - [25] Juan P. Torres, Optical communications: Multiplexing twisted light, *Nat. Phot.* **6**, 420 (2012).
 - [26] A. Kolmogorov, Sulla determinazione empirica di una legge di distribuzione, *G. Ist. Ital. Attuari.* **4**, 83 (1933).
 - [27] N. Minorsky, Directional stability of automatically steered bodies, *J. Amer. Soc. Naval Eng.* **34**, 280 (1922).
 - [28] H. T. Friis, Introduction to radio and radio antennas, *IEEE Spectr.* **8**, 55 (1971).
 - [29] S. B. Alexander, *Optical Communication Receiver Design* (SPIE Optical Engineering Press, Bellingham, Washington, USA, 1997).
 - [30] Abhijit Biswas, Joseph M. Kovalik, Malcolm W. Wright, and William T. Roberts, in *Proc. of SpaceOps 2014 Conf.*, Vol. 1710 (AIAA, 2014).
 - [31] Mo Chen, Chao Liu, and Hao Xian, Experimental demonstration of single-mode fiber coupling over relatively strong turbulence with adaptive optics, *App. Opt.* **54**, 8722 (2015).
 - [32] Daniel F. V. James, Paul G. Kwiat, William J. Munro, and Andrew G. White, Measurement of qubits, *Phys. Rev. A* **64**, 052312 (2001).
 - [33] Christopher Granade, Joshua Combes, and D. G. Cory, Practical bayesian tomography, *New J. Phys.* **18**, 033024 (2016).

- [34] Christopher Ferrie and Robin Blume-Kohout, Maximum likelihood quantum state tomography is inadmissible, arXiv:1808.01072 (2018).
- [35] J. C. Chapman, H. Bernstein, K. Meier, C. Zeitler, and P. G. Kwiat, in *Proc. SPIE 10547*, Vol. 10547 (SPIE, San Jose, CA, 2018).
- [36] H. Buhrman, R. Cleve, J. Watrous, and R. de Wolf, Quantum Fingerprinting, *Phys. Rev. Lett.* **87**, 167902 (2001).
- [37] Ivan Marcikic, Hugues de Riedmatten, Wolfgang Tittel, Valerio Scarani, Hugo Zbinden, and Nicolas Gisin, Time-bin entangled qubits for quantum communication created by femtosecond pulses, *Phys. Rev. A* **66**, 062308 (2002).
- [38] B. S. Shi and A. Tomita, Generation of a pulsed polarization entangled photon pair using a sagnac interferometer, *Phys. Rev. A* **69**, 013803 (2004).
- [39] T. Kim, M. Fiorentino, and F. N. C. Wong, Phase-stable source of polarization-entangled photons using a polarization sagnac interferometer, *Phys. Rev. A* **73**, 012316 (2006).
- [40] Kevin Zielnicki, Karina Garay-Palmett, Daniel Cruz-Delgado, Hector Cruz-Ramirez, Michael F. O'Boyle, Bin Fang, Virginia O. Lorenz, Alfred B. U'Ren, and Paul G. Kwiat, Joint spectral characterization of photon-pair sources, *J. Mod. Opt.* **65**, 1141 (2018).
- [41] Joseph C. Chapman, Trent Graham, Francesco Marsili, Matthew Shaw, Christopher Zeitler, and Paul G. Kwiat, in *Proc. of OSA Conf. on Lasers and Electro-Optics* (2017), p. FTu4F–3.
- [42] A. Einstein, Zur elektrodynamik bewegter körper, *Ann. Phys.* **322**, 891 (1905).